Combined XPS / TEM study of the chemical composition and structure of the passive film formed on additive manufactured 17-4PH stainless steel

Adrien Barroux, Thomas Duguet, Nadège Ducommun, Eric Nivet, Julien Delgado, Lydia Laffont, Christine Blanc

Combined XPS / TEM study of the chemical composition and structure of the passive film formed on additive manufactured 17-4PH stainless steel

Adrien Barroux [a,b], Thomas Duguet [a], Nadège Ducommun [b], Eric Nivet [b], Julien Delgado [c], Lydia Laffont [a,*], Christine Blanc [a]

[a] CIRIMAT, Université de Toulouse, CNRS, INP-ENSIACET, 4 allée Emile Monso, BP 44362, 31030 Toulouse cedex 4, France
[b] CETIM, Pôle Matériaux Métalliques et Surfaces, 74 route de la Jonelière CS 50814, 44308 Nantes, France
[c] CETIM, Pôle Matériaux Métalliques et Surfaces, 52 Avenue Félix Louat CS 80067, 60304 Senlis, France

Keywords:
A. Stainless steel
B. XPS
B. STEM
C. Passive films
Laser Beam Melting

A B S T R A C T

The structure and chemical composition of the passive film formed on 17-4PH martensitic stainless steel (MSS) manufactured by powder bed laser beam melting (LBM) were investigated combining XPS and TEM analyses, by comparison to a conventional 17-4PH. The structure of the passive film was found similar for both MSSs, with, on the matrix, a duplex layer composed of Fe and Cr oxy-hydroxide followed by an intermediate layer enriched in metallic compounds. A particular Nb oxide film formed on the NbC precipitates merging to the surface for both MSSs. Significant differences in thickness and Cr distribution were observed between both MSSs.

1. Introduction

Precipitation hardening martensitic stainless steels (MSSs), such as 17-4PH MSS, arise from an incremental industrial steel development with the aim of combining good corrosion resistance and high mechanical properties. These properties enable 17-4PH MSS to be used in numerous industrial applications such as nuclear power plants, aircraft components, or biomedical tools. They are provided by appropriate thermal treatments, i.e. a solution annealing heat treatment which homogenises the chemical element content, followed by an ageing heat treatment which allows the precipitation of secondary hardening phases. In the case of 17-4PH MSS, the ageing treatment generates the nanoscale precipitation of fine copper-rich precipitates, the nucleation and growth of niobium carbides (NbCs) precipitates and the reversion of secondary austenitic phase [1–5]. Those microstructure evolutions are controlled by the temperature and the duration of the ageing treatment, which allow the alloy to reach the required mechanical properties. In this way, the mastery of the microstructure and subsequent in-service properties give 17-4PH MSS a great versatility with a large field of applications.

17-4PH is a good candidate for additive manufacturing and particularly laser beam melting (LBM) process with the aim of extending the industrial applications of this material. The benefits of LBM are numerous: layer-by-layer build-up of 3D structures with new manufacturing and geometry possibilities. But, several recent studies have been focused on the relationship between the microstructure, the manufacturing parameters, the mechanical properties and the post thermal treatment of LBM 17-4PH MSS [6–11]. Results showed specific properties and complex mechanical tensile response depending on the loading direction for the final LBM parts as compared to the conventional 17-4PH MSS, associated with a peculiar LBM microstructure. Moreover, the final microstructure, the mechanical and corrosion properties of the LBM parts were found to depend significantly on the LBM parameters. Indeed, many studies highlighted the effect of the scan strategy used to melt the powder bed and the energy density brought by the laser as the main origins of the microstructure and manufacturing defects (e.g. gas pores, lack-of-fusion pores, oxide inclusions) [9,12–15]. The chemical composition and the microstructure of the initial powder grains also strongly influence the properties of the final parts [16,17]. Murr et al. demonstrated that 17-4PH parts fabricated with either argon or nitrogen-atomised powder under argon protective gas are mainly composed of martensitic phase, whereas those fabricated with nitrogen-atomised powder under nitrogen gas are mainly composed of austenite [17]. In addition, Meredith et al. showed that phase equilibrium changed with the gas used (during both powder atomisation and manufacturing) inducing chemical enrichment or depletion in some alloying elements [18]. For example, a nitrogen enrichment could be observed in both the powder and the final part leading to a stabilisation

* Corresponding author.
E-mail address: lydia.laffont@ensiacet.fr (L. Laffont).

https://doi.org/10.1016/j.surfin.2020.100874

of the austenitic phase by lowering the martensitic start temperature (M_s) [3,8,18].

Concerning the corrosion behaviour of the LBM 17-4PH and the 15-5PH MSSs, there are only a few works in the literature [19,20]. But more numerous data can be found concerning austenitic stainless steel like 316L; for example Tobar et al. pointed out the importance of initial powder quality on the corrosion behaviour, and in particular the detrimental effect of secondary alloying elements such as Mn [21]. Chao et al. showed an increase in pitting corrosion resistance for LBM 316L stainless steel as compared to a conventional material [22]. The more positive pitting potential values were attributed to smaller MnS inclusions present in the LBM MSS than in the conventional counterpart. In addition, data from the literature proposed a relationship between typical manufactured defects generated by the LBM process and the corrosion behaviour of LBM parts. For a 316L austenitic stainless steel too, Laleh et al. showed that lack-of-fusion pores – which are already detrimental to mechanical properties such as the fatigue lifetime – are also detrimental to the corrosion resistance [23]. They also demonstrated that Si-rich oxide inclusions could drastically reduce the pitting corrosion resistance depending on their size and shape, and could also act as preferential pit initiation sites [24].

Finally, this brief literature review shows that LBM process and the post thermal treatment generate different microstructures which can lead to different corrosion behaviour. Indeed, it is well-known for various conventional stainless steels that changes in the microstructure can induce different corrosion mechanisms and can influence the susceptibility to pitting corrosion and/or intergranular corrosion for example [25–29]. Moreover, the pitting corrosion resistance of metallic materials is controlled by a passive film generally described as a thin oxide layer covering the alloy [27,30]. Numerous breakdown models were proposed to explain the formation, the steady state and the breakdown of passive films. The mechanisms of the passivity breakdown were thoroughly studied by Macdonald for many years with the development of the Point Defect Model (PDM) [31–34]. Others, such as Marcus et al. proposed a more complex model of pitting corrosion initiation based on atomic force microscopy (AFM) observations of a nanoscale passive film on nickel [35]. Although there is no consensus, the passivity breakdown seems linked to local passive film defects (grain boundaries, vacancies), but also to the structure and the chemical composition of the passive film and those of the alloy underneath [30,36,37]. The structure and the chemical composition of passive films were analysed for austenitic stainless steels by auger emission spectroscopy (AES), X-ray photoelectron spectroscopy (XPS), time-of-flight secondary ion mass spectrometry (TOF-SIMS) or transmission electron microscopy (TEM) [38–43]. The passive film was described as a nanoscale bilayer of Cr^{III} and Fe^{III} oxide / hydroxide with the presence of secondary alloying elements depending on the stainless steels. However, we suggest that the particular LBM microstructures could lead to differences in passive film structure and chemistry and therefore in the pitting corrosion resistance by comparison to the conventional counterpart.

We showed, in a previous study on the corrosion behaviour of 17-4PH MSS manufactured by LBM, significant differences in the pitting susceptibility between LBM and conventional samples in NaCl solution [44]. A more positive pitting potential value was observed for the 17-4PH LBM MSS; this was attributed, at least partially, to smaller NbC precipitates, which acted as preferential pit initiation sites, in agreement with Clark et al. [45]. Results also showed that lack-of-fusion pores were preferential pit initiation sites, but they did not have a detrimental influence on the pitting corrosion resistance of the LBM MSS due to their very low amount in the samples. Moreover, the influence of small gas pores was assumed to be negligible. However, a greater susceptibility to metastable pitting was observed for the LBM MSS as compared to the conventional samples. Results suggested differences in the properties of the passive films formed on LBM and conventional steels. But the relationship between the alloy microstructure, the features of the passive film and the corrosion behaviour was out of the scope of this study. Thus, in the present work, a combination of TEM and XPS analyses was performed to study the passive film formed on LBM 17-4PH MSS after exposure to a NaCl solution by comparison to the passive film formed on the conventional counterpart. Attention was paid to the chemical composition, structure and thickness of the passive film, with specific attention to the passive film formed on NbC precipitates, considering the significant influence of these precipitates on the pitting corrosion resistance. The electrochemical response of the passive films was out of the scope of this study, and will be the topics of a forthcoming study. The results concerning the passive film structure and chemical composition were analysed by considering the microstructure of the alloys underneath and by referring to their pitting behaviour.

2. Experimental procedure

2.1. Sample preparation

17-4PH MSS parts were additively manufactured by LBM process using an EOS M290 machine equipped with a 400 W laser under argon atmosphere. Cubic LBM samples were built from 17-4PH Erasteel powder (average diameter of 33 μm) on a building plate maintained at 200 °C with 40 μm of bed powder thickness. The orientation of each sample on the building plate was identified, considering the three characteristic planes of the cubic samples, with XY that corresponded to the building plate plane and Z to the building direction. For brevity reasons, most of the results were given for XY sample; however, when needed, results for XZ and YZ planes were also reported. A 50-mm wrought cylinder of 17-4PH MSS processed by conventional metallurgy was used as reference (Böhler Edelstahl). Chemical compositions of both MSSs determined by spark optical emission spectroscopy are shown in Table 1. Slight differences are noticed between the LBM and conventional samples, especially for the Si content, which is twice higher for the LBM samples; a quite similar Cr content and same Nb content were also observed. Conventional and LBM MSSs were heat treated following the ASTM A564 standard for conventional 17-4PH MSS. The heat treatment is composed of a solution annealing treatment at 1040 °C for 30 min followed by air quenching; then the samples were aged at 480 °C for 1 h and air quenched, which corresponds to H900 standardised ageing.

The microstructures of conventional and LBM MSSs have been described in details in a previous article [44]. Only the main results are reminded here in order to help in understanding the analyses of the passive films below. The LBM MSSs have a finer microstructure characterised by finer martensite laths (width of 50 – 800 nm, and 700 nm – 2.5 μm for the LBM and conventional MSSs, respectively) and finer NbCs precipitates. The amount of austenite was between 8 and 12 % for LBM MSSs, depending on the planes, whereas it was only 0.8 % for the conventional MSS. Finally, LBM MSSs contained coarser Cu-rich precipitates than the wrought MSS.

For electrochemical experiments, coupons of *ca.*1 cm^2 surface area exposed to the electrolyte were cut in the core of the sample, for both LBM and conventional samples. The coupon surfaces were then polished with SiC paper down to grade 2400 and mirror-finished with 6 μm, 3 μm and 1 μm diamond paste; then, they were rinsed with deionised water and dried under hot air flow. An electric wire was stuck on the back of the coupons with silver conductive adhesive paste and isolated with silicone seal for electric connection. Then, the coupons were immersed for 1 h in 0.5 M NaCl solution so that they reached quasi steady state conditions. This allowed the corrosion potential value (E_{corr}) to be measured; samples were then polarised at +150 $mV_{/Ecorr}$ for 30 min to make the passive films grow on their surface. The coupons were finally rinsed with deionised water, sonicated in acetone and ethanol and dried under air flow.

Table 1
Chemical composition of the 17-4PH samples used in this study.

Element wt%	Cr	Ni	Cu	C	Nb	Si	Mo	N	S	P	Fe
ASTM A654	15.0 – 17.0	3.0 – 5.0	3.0 – 5.0	≤ 0.07	0.15 – 0.45	≤ 1	-	-	≤ 0.030	≤ 0.040	bal.
wrought cylinder (conventional)	15.42	4.49	3.24	0.036	0.26	0.35	0.15	0.030	≤ 0.005	0.016	bal.
LBM parts	16.20	4.08	3.56	0.028	0.27	0.71	< 0,02	0.035	≤ 0.005	0.007	bal.

Chemical composition of the 17-4PH samples used in this study compared to the ASTM A564 standard.

2.2. XPS analyses

XPS analyses were carried out on a Thermo Kalpha apparatus, equipped with a monochromatised Al-Kα source (hν = 1486.6 eV). The X-ray spot surface area was approximately 400 μm in diameter. All photoelectron spectra were analysed with built-in Avantage software (Thermo). A Shirley background was systematically subtracted. Survey spectra and high-resolution spectra were recorded with a 150 eV and a 30 eV pass energy, respectively. Depth profiles were performed upon Ar^+ etching on high-resolution Fe 2p, Cr 2p, Nb 3d and O 1s spectra. A pass energy of 60 eV was found to be the best compromise between resolution and time for the acquisition of the profiles. Metallic Fe, Fe_2O_3 oxide, metallic Cr and Cr_2O_3 chromine reference samples were used to decompose Fe and Cr spectra. A 30/70 Lorentzian/Gaussian ratio was used to fit all peaks, occasionally including asymmetry parameters for metallic components.

2.3. TEM analyses

Cross-section thin foils of the passive film were prepared using a FEI dual beam HELIOS nanolab 600i at UMS Castaing (Toulouse, FR). A protective carbon layer was deposited with FIB-SEM before cutting the TEM samples to avoid scaling of the oxide layers. TEM and scanning TEM (STEM) imaging was performed on a JEOL cold-FEG JEM-ARM200F operated at 200 kV equipped with a Cs corrector probe of 0.78 Å spatial resolution. Characterisations of the passive films were done using the bright field (BF) and the high-angle annular dark field (HAADF) STEM modes. Energy dispersive X-ray spectroscopy (EDS) was used to analyse the evolution of the chemical composition across the passive film-alloy interface. EDS qualitative maps and line scans of the sample were acquired with a JEOL CENTURIO SDD detector.

3. Results and discussion

3.1. Global approach of the structure and chemical composition of the passive films

Cross-sectional views of the passive films observed by TEM bright field imaging for the conventional and the LBM (plane XY parallel to the building plate) 17-4PH MSS samples thermally treated in the H900 condition are shown in Fig. 1. As indicated in the experimental part, the passive film is formed during exposure to a 0.5 M NaCl solution under potentiostatic polarisation at +150 $mV/_{Ecorr}$ on polished surfaces. A protective carbon layer was deposited with FIB-SEM before cutting the TEM samples to avoid scaling of the oxide layers. The passive films were found homogenous in thickness and amorphous (lack of order at atomic level); they covered the whole surface for both analysed samples. In a first global approach, the thickness of the passive films was estimated to be around 3 nm for both samples as expected for stainless steels. These observations are in good agreement with the Oh et al.'s TEM study of the passive film formed on a Fe-20Cr-10Ni stainless steel [42] and Yue et al.'s study on a 316L SS [46].

To complete TEM imaging with data concerning the chemical composition of the passive film, XPS analyses were performed on the passive films formed on the 17-4PH MSSs. Figs. 2 and 3 compiled the high-resolution surface spectra of Fe 2p, Cr 2p, Cu $2p_{3/2}$, Ni $2p_{3/2}$, O 1s, C 1s, Nb 3d and Si 2p recorded on conventional and LBM XY samples, respectively. In addition, parameters used to fit the XPS spectra for conventional and LBM XY samples are given in Table 2. For comparison purpose and to complement literature data, results obtained for LBM XZ and YZ samples are also reported in Table 2. The Fe $2p_{3/2}$ and Cr $2p_{3/2}$ core levels were decomposed for the conventional (Fig. 2a and b) and the LBM XY (Fig. 3a and b) samples. The spectra for both the conventional and the LBM (all planes) MSSs are composed of a broad oxide/hydroxide peak coupled with metal peak, suggesting that the passive films are mainly composed of thin Fe and Cr oxide layer. Indeed, Biesinger et al. studied various transition metallic, oxide and hydroxide components by XPS (*e.g.* Fe, Cr, Ni or Cu), and demonstrated that the broad shape for Fe and Cr oxides results from multiplet splitting of the

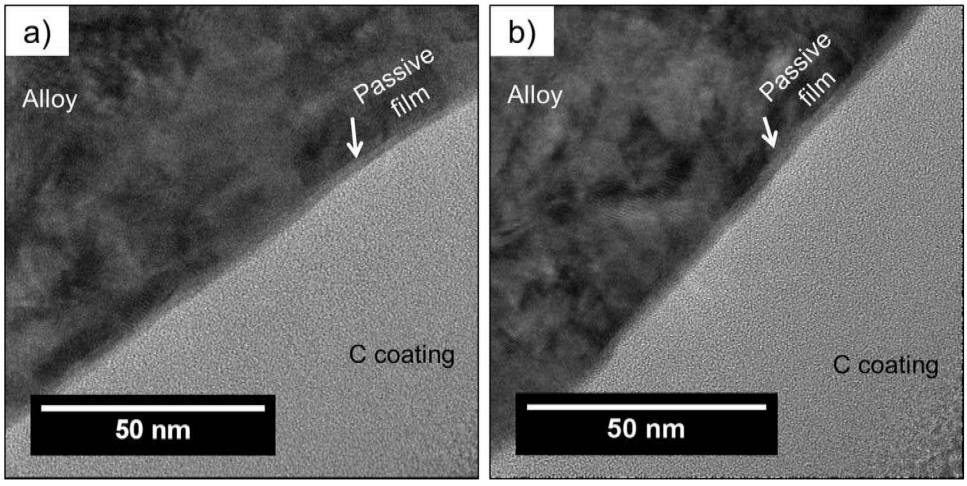

Fig. 1. TEM bright field images of the passive film formed on the conventional (a) and LBM XY (b) MSS samples in 0.5 M chloride solution.

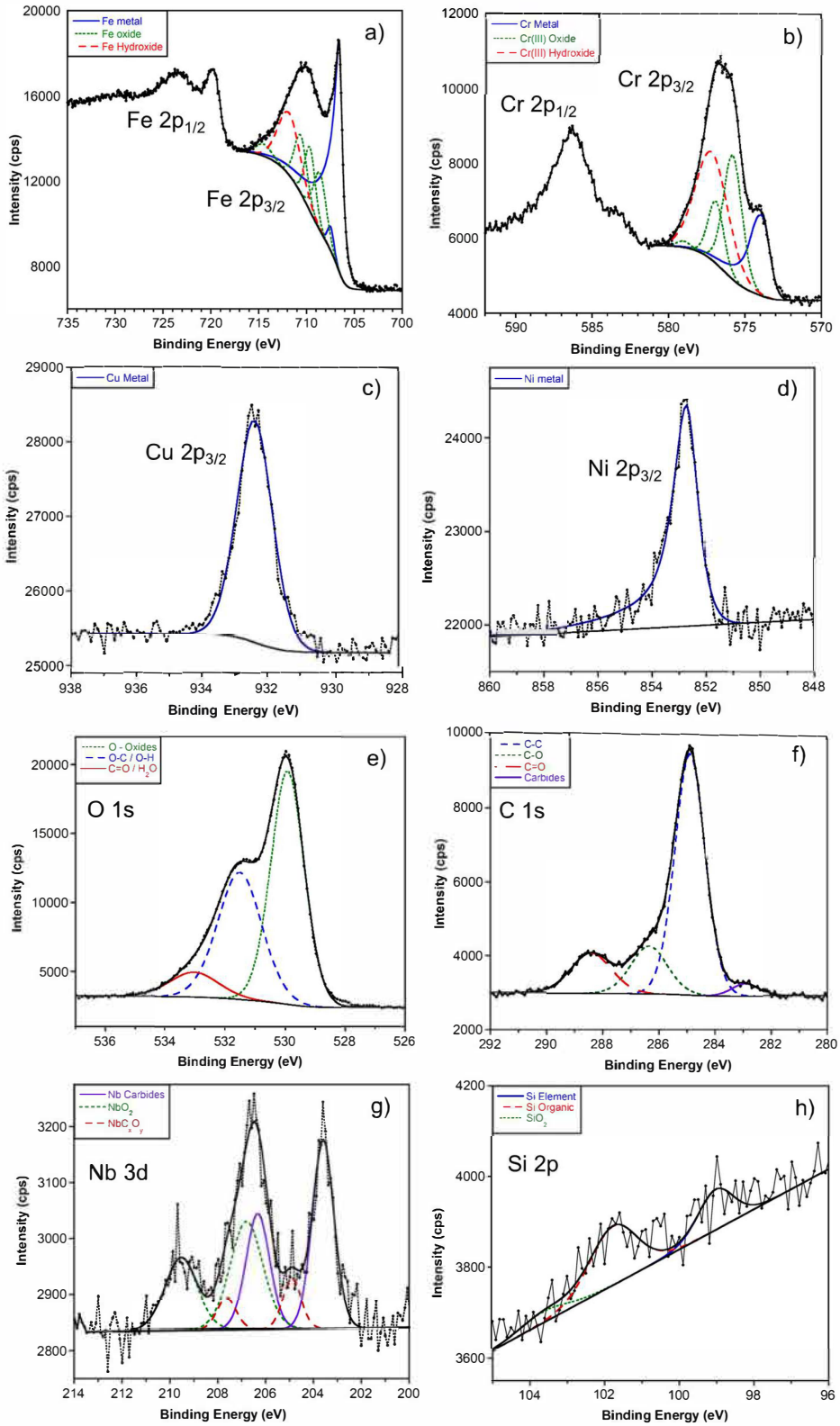

Fig. 2. High-resolution spectra of Fe 2p, Cr 2p, Cu 2p, Ni 2p, O 1s, C 1s, Nb 3d and Si 2p with their fitted components contribution for conventional sample.

core levels due to the interaction of the photoelectrons with the unpaired outer shell electron [47,48]. In this respect, Fe $2p_{3/2}$ peaks were fitted with two metallic split components (ΔE_{metal} = 0.9 eV), four oxides multiplets and one broad hydroxide component (Table 2). This complex multiplet splitting structure could not allow the distinction between Fe^{II} and Fe^{III} oxide species. A similar peak fitting was used for Cr $2p_{3/2}$ with one metallic, three oxides and one broad hydroxide components for all four samples. The binding energy (BE) Cr $2p_{3/2}$ values (between 575 and 578 eV) for oxide and hydroxide peaks correspond to Cr^{III} components and were attributed to Cr_2O_3 and $Cr(OH)_3$ species. As said previously for Fe oxide components, the determination of the oxide/hydroxide proportion could not be made because of the multiple overlap between

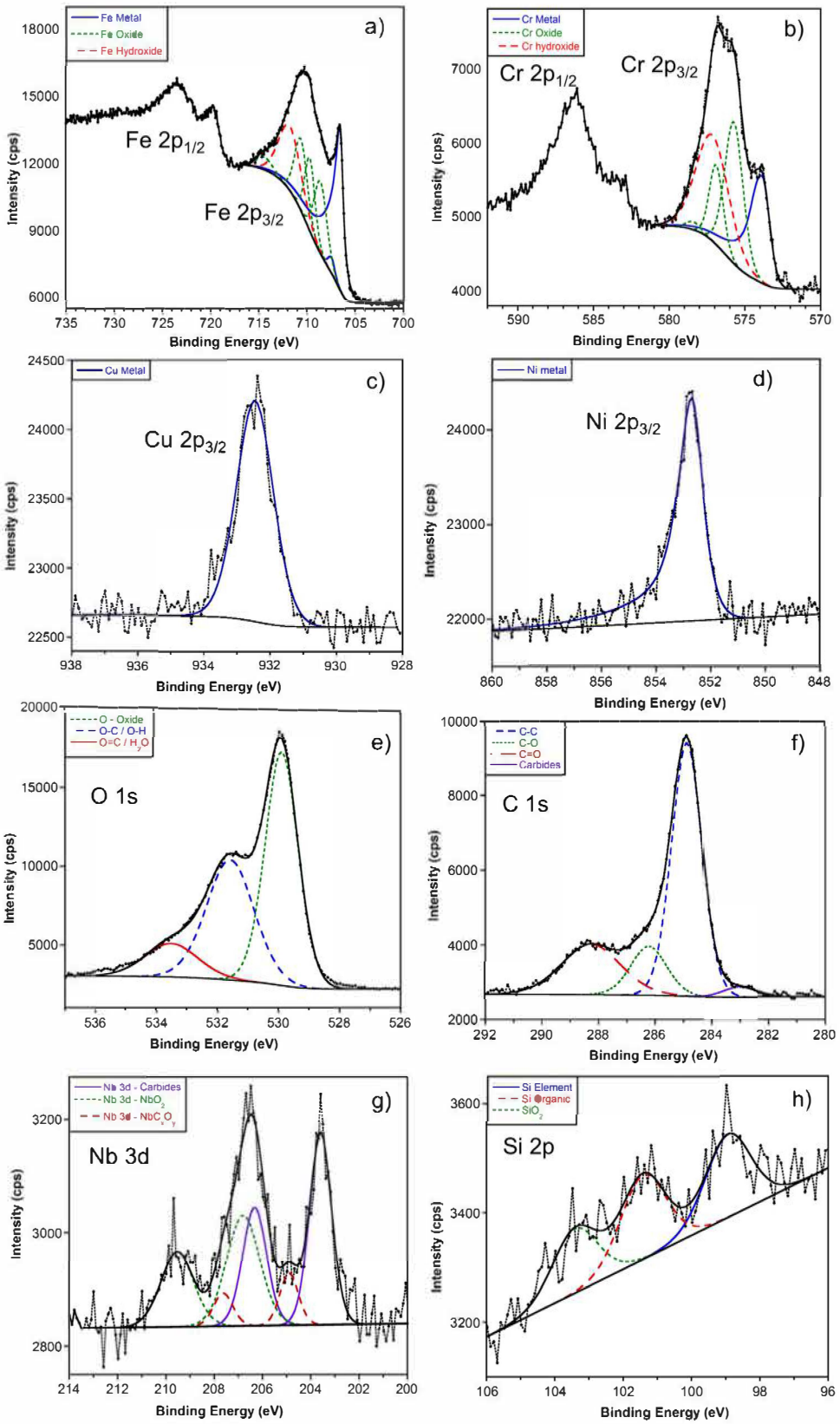

Fig. 3. High-resolution spectra of Fe 2p, Cr 2p, Cu 2p, Ni 2p, O 1s, C 1s, Nb 3d and Si 2p with their fitted components contribution for LBM XY sample.

oxide and hydroxide peaks in a short BE range (*i.e.* from 706 to 712 eV and from 573 to 578 eV for Fe $2p_{3/2}$ and Cr $2p_{3/2}$, respectively). This interpretation of Fe $2p_{3/2}$ and Cr $2p_{3/2}$ spectra is simplified in order to avoid misinterpretation but still retains relevant information. The high-resolution spectra of Cu $2p_{3/2}$ and Ni $2p_{3/2}$ for the conventional (Fig. 2c and d) and the LBM XY (Fig. 3c and d) samples include only one asymmetric peak for each element with a BE value around 852.2 eV for Ni and 932.5 eV for Cu, which are therefore metallic. Similar results

Table 2
Binding energy, full with at half maximum (FWHM) and relative area of the assign peaks used to analyse XPS high-resolution spectra on conventional and LBM MSSs after anodic potentiostatic polarisation in 0.5 M chloride solution.

		conventional			LBM XY			LBM XZ			LBM YZ		
Core level	Assignment	BE (eV)	FWHM (eV)	Relative area	BE (eV)	FWHM (eV)	Relative area	BE (eV)	FWHM (eV)	Relative area	BE (eV)	FWHM (eV)	Relative area
Fe $2p_{3/2}$	Fe metal	706.6	0.8	1.00	706.6	0.8	1.00	706.6	0.8	1.00	706.6	0.8	1.00
	Fe metal (ΔE_{metal} = 0.9 eV)	707.5	0.8	0.04	707.5	0.8	0.04	707.5	0.8	0.06	707.5	0.8	0.04
	Fe oxide peak 1	708.6	1.6	0.21	708.6	1.6	0.37	708.6	1.6	0.37	708.6	1.6	0.26
	Fe oxide peak 2	709.7	1.4	0.20	709.7	1.3	0.30	709.8	1.5	0.46	709.8	1.5	0.33
	Fe oxide peak 3	710.6	1.6	0.21	710.6	1.6	0.37	710.8	1.6	0.32	710.9	1.6	0.25
	Fe oxide peak 4	714.5	2.0	0.05	714.4	2.0	0.08	714.5	2.0	0.08	714.5	2.0	0.05
	Fe hydroxide	711.8	2.8	0.40	711.8	2.8	0.58	712.0	2.8	0.55	712.0	2.8	0.42
Cr $2p_{3/2}$	Cr metal	573.9	1.2	0.53	573.9	1.2	0.74	574.0	1.2	0.48	573.9	1.2	0.63
	Cr^{III} oxide peak 1	575.8	1.5	0.66	575.7	1.5	0.75	575.7	1.6	0.92	575.8	1.5	0.68
	Cr^{III} oxide peak 2	576.9	1.3	0.28	576.9	1.1	0.32	576.9	1.3	0.32	576.9	1.4	0.38
	Cr^{III} oxide peak 3	579.0	1.1	0.03	578.4	1.1	0.03	578.9	1.1	0.03	578.8	1.6	0.05
	Cr^{III} hydroxide	577.2	2.6	1.00	577.2	2.6	1.00	577.2	2.7	1.00	577.2	2.8	1.00
Nb 3d	Nb carbides (5/2)	203.6	1.0	1.00	203.6	1.1	1.00	203.6	0.9	1.00	203.6	1.0	0.95
	Nb carbides (3/2)	206.3	1.1	0.67	206.3	1.2	0.67	206.3	1.0	0.67	206.3	1.1	0.64
	NbC_xO_y (5/2)	204.8	0.9	0.15	204.9	0.9	0.23	204.9	1.3	0.43	204.9	1.5	0.37
	NbC_xO_y (3/2)	207.5	0.9	0.10	207.6	1.0	0.15	207.6	1.3	0.29	207.7	1.6	0.24
	$Nb^{IV}O_2$ (5/2)	206.9	2.0	0.83	206.8	1.7	0.86	206.7	1.3	0.80	206.9	1.4	1.00
	$Nb^{IV}O_2$ (3/2)	209.6	1.9	0.56	209.5	1.7	0.58	209.4	1.2	0.54	209.6	1.4	0.67
O 1s	Metal oxides	529.9	1.4	1.00	529.9	1.3	1.00	529.9	1.3	1.00	529.8	1.4	1.00
	O-H (hydroxides) / C-O	531.5	1.8	0.72	531.4	1.9	0.74	531.5	1.9	0.67	531.3	1.9	0.83
	H_2O / CO_2 / SiO_2	533.0	2.0	0.16	533.8	2.1	0.23	532.9	2.1	0.13	532.6	2.1	0.46
Ni $2p_{3/2}$	Ni metal	852.7	1.1	1.00	852.8	1.1	1.00	852.7	1.1	1.00	852.8	1.1	1.00
Cu $2p_{3/2}$	Cu metal	932.4	1.3	1.00	932.5	1.4	1.00	932.5	1.3	1.00	932.4	1.2	1.00
Si 2p	Si element	98.9	1.2	0.51	99.1	1.2	0.82	99.0	1.2	0.58	99.0	1.1	0.43
	Si organic	101.7	1.5	1.00	101.7	1.5	1.00	101.8	1.5	1.00	101.8	1.5	1.00
	$Si^{IV}O_2$	103.6	1.6	0.19	103.4	1.6	0.76	103.4	1.4	0.27	103.4	1.5	0.75
C 1s	C Niobium carbides	282.9	1.2	0.05	283.0	1.3	0.04	283.1	1.3	0.04	283.0	1.3	0.04
	C-C (adventitious)	284.9	1.3	1.00	284.9	1.3	1.00	284.8	1.3	1.00	284.9	1.4	1.00
	C-O	286.3	1.6	0.24	286.2	1.7	0.29	286.4	1.7	0.20	285.4	1.7	0.26
	C=O	288.4	1.8	0.23	288.3	1.8	0.29	288.5	1.8	0.19	287.9	1.8	0.16

Binding energy, full with at half maximum (FWHM) and relative area of the assign peaks used to analyse XPS high-resolution spectra on conventional and LBM MSSs after anodic potentiostatic polarisation in 0.5M chloride solution.

were obtained for LBM XZ and YZ samples (Table 2). The metallic state for Cu $2p_{3/2}$ is confirmed using the modified Auger parameters α'. The formula is given by the Eq. (1), which result allows Cu^0, Cu^I and Cu^{II} to be clearly distinguished [49]:

$$\alpha' = KE(CuLMM) + BE\left(Cu2p_{3/2}\right) \quad (1)$$

where KE (Cu LMM) corresponds to the kinetic energy of the Auger LMM transition and BE (Cu $2p_{3/2}$) corresponds to the binding energy of the Cu $2p_{3/2}$ peak. Thereby, for the conventional and all the three LBM samples, α' exhibits a mean value of 1851.5 eV, i.e. Cu is metallic (Cu^0) [47,49]. Then, the O 1s spectrum for conventional (Fig. 2e) and LBM XY (Fig. 3e) is decomposed in three peaks with numerous contributions. A first peak at low BE value around 529.9 eV corresponding to metal oxides (O^{2-}), a second peak around 531.4 eV corresponding to metal hydroxides (OH^-) and organic ketone (C-O bond), and finally a broad peak at higher BE value corresponding to adsorbed water, carbon dioxides (C=O bond) and SiO_2. Organic ketone, carbon dioxide and adsorbed water peaks are associated with organic contamination due to preparation, electrochemical tests (use of silicone seal) and acetone/ethanol cleaning. Organic contamination is also present on C 1s spectra on both conventional and LBM MSS samples (Figs. 2f and 3f, respectively) with three characteristic peaks attributed to C-C bonds (BE around 284.9 eV), C-O bonds (BE around 286.3 eV) and C=O bonds (BE around 288.3 eV). A fourth peak at lower BE value is attributed to C-Nb bond (around 283.0 eV) arising from NbC precipitates inside the MSSs for both conventional and LBM XY samples (same results for XZ and YZ samples). The NbC precipitates contribution is found again on the Nb 3d spectra (Figs. 2g and 3g) convoluted with other Nb oxide species due to spin-orbit splitting ($\Delta E_{Nb\ 3d} \approx 2.7$ eV) [50]. Gupta et al. demonstrated that NbC compounds present complex oxide layers at different oxidation degrees in the case of NbC nanocomposites [51]. Based on this work, the Nb 3d spectra were decomposed in three components (six peaks for $3d_{5/2}$ and $3d_{3/2}$) corresponding respectively to NbC precipitates at lower BE values, a mixture of carbide-oxide NbC_xO_y and $Nb^{IV}O_2$ oxide at higher BE values for all samples studied. This could suggest that NbC precipitates are oxidised in stable Nb^{IV} state during the passive film formation with a transition NbC_xO_y layer between the NbC precipitates and the $Nb^{IV}O_2$ stable oxide. Finally, the Si 2p high-resolution spectra (Figs. 2h and 3h) were decomposed in three simple components because of the low spin-orbit coupling energy difference ($\Delta E_{Si\ 2p} \approx 0.6$ eV). The peak at lower BE value (around 99.0 eV) is assigned to Si element dissolved in the martensitic matrix, the second peak corresponds to Si organic contamination due to silicon seal (around 101.8 eV) and the last peak (around 103.4 eV) corresponds to Si^{IV} and was attributed to SiO_2. Nevertheless, it could be noticed a non-negligible contribution of the SiO_2 for the LBM XY samples on Si 2p high-resolution spectra (Fig. 3h) and for LBM XZ and YZ samples (Table 2), whereas there is almost no contribution of SiO_2 peak for the conventional one. This SiO_2 is assumed to correspond to Si-rich oxide inclusions formed during the LBM process between two lased layers as described in previous work [9,44,52]. Therefore, the presence of SiO_2 on the Si 2p spectra arises from the

underlying alloy only for LBM samples and is not part of the passive film.

Chemical quantification of the different alloying elements was performed from the high-resolution XPS spectra peak fitting. The information depth included both the passive layer and the alloy underneath. The result of the elemental quantification is given in Table 3 in atomic percent for conventional and all three LBM samples. The presence of organic contamination on the passive film surface can be shown with the high carbon content and slightly higher content for Si as compared to the nominal composition of the alloy (Table 1). For all samples, the oxygen concentration is greater than 40 at.%, indicating that most of the XPS signal arises from the passive film. Fe and Cr are the main oxide components and have a moderate concentration which is lower than the nominal alloy composition due to high C and O content. Nevertheless, the Cr content is significantly higher for the conventional sample (8 at. %) than for the LBM samples (5 at.% whatever the LBM plane). The calculation of the relative Cr/Fe ratio gives 0.59 for the conventional sample against 0.37, 0.36 and 0.46 for the LBM XY, XZ and YZ, respectively, which confirms that the passive film formed on the conventional sample contains more Cr than the LBM ones. The Cr/Fe ratios were found very low (<1) as compared to what could be obtained from study on austenitic stainless steel, probably due to the lower Cr content in the nominal 17-4PH composition [39–41]. The differences in Cr content for the passive films formed on LBM and conventional MSSs could be explained by referring to the austenite content of the samples. Indeed, we showed in a previous study [44] that the austenite content was between 8 and 12 % and only 0.8 % for the LBM and conventional samples, respectively. Langberg et al. [53] recently showed, for a super duplex stainless steel, that the passive film formed on ferrite had a higher Cr content than this one formed on austenite due to the higher Cr content in ferrite. In the present study, similar differences in Cr content were likely to exist between martensite and austenite, with higher Cr content in martensite, due to the fact that most part of the austenite was reversed austenite. Therefore, it was assumed here that the lower martensite to austenite ratio for LBM MSSs could contribute to explain the lower Cr content in the passive films formed on these samples. As expected, quantification of Cu and Ni exhibits poor values (≤1 at%) with a slightly higher content for the conventional sample. It could also be noticed that Nb content is quite similar to the nominal composition of the 17-4PH due to the presence of Nb oxide in the passive film.

In summary, first TEM observations (Fig. 1) showed that the thicknesses of the passive films formed in NaCl solution on the conventional and LBM MSSs samples were similar: the oxide layers were thin (~3 nm) and amorphous. XPS analyses showed that passive films were composed of a mixture of Fe and Cr^{III} oxy/hydroxide, with the presence of Nb oxides in small amount. However, the chemical composition of the passive films differed between the conventional and the LBM MSSs samples, especially for the Cr content which was higher for the conventional MSS probably due to its lower content in reversed austenite. Concerning the different planes of the LBM parts, no significant differences were observed. Nevertheless, studies from the literature often described the passive films formed on stainless steels as duplex layers, *i.e.* composed of an inner and an outer layer with different chemical compositions [39,41,54]. Hence, in order to obtain additional data on the passive films, their chemical composition and structure were then studied with XPS depth profiles and STEM-EDS analyses at the nanometre scale.

3.2. Analysis of the structure and chemical composition of the passive films at the nanometre scale

In order to provide a better insight into the structure and chemical composition of the passive films formed on both MSSs, STEM-EDS analyses and XPS depth profiles were combined. Fig. 4 shows STEM bright field (BF) imaging at nanometre scale of the passive films formed on the conventional (4a) and LBM XY (4b) 17-4PH MSSs. Such analyses were performed only for the LBM XY sample and not for the other LBM planes considering the complexity of the STEM technique and taking into account similar XPS results. EDS analyses performed in zones marked by the white boxes in Fig. 4 (area of 2.3 × 0.75 nm^2) gave access to the chemical quantification of the different layers constitutive of the passive films. Here, it is of major importance to note that each box is assumed to correspond to specific regions of the passive film and/or the alloy underneath; however some lack of accuracy on the location of the EDS zones could not be neglected with respect to the complexity of the technique. Moreover, the EDS quantification constitutes a mean analysis on the whole zone of the studied boxes, hence improving the signal-to-noise ratio. Boxes were numbered from 1 to 4 in Fig. 4. For the conventional alloy, the boxes 1 and 2 were assumed to correspond to the passive film at different depths from the external surface i.e. in the outer and inner layer, respectively; the third and fourth boxes were attributed to the alloy. The fourth zone was considered as reference as it was located in the bulk of the alloy. For the LBM XY sample, boxes 1 to 4 were attributed to the outer layer, the inner layer, the intermediate layer and the bulk alloy, respectively. The intermediate layer was defined as the interface between the passive film and the alloy. For the conventional sample, this contribution was not detected due to the location of the boxes and the small thickness of the intermediate layer. Results from EDS analyses are given in Table 4. Due to the amorphous nature of the passive films, the results of the EDS analyses were considered with comparison purpose only. The first EDS analyses took into account the oxygen signal. For both MSSs, the oxygen content was maximum in boxes 1 and 2 corresponding to the passive film, then decreased in the box 3 and finally dropped down to zero in box 4, i.e. in the bulk alloy. Concerning the alloying elements, increasing values of Cr, Ni and Cu from boxes 1 to 2 for both samples confirmed the presence of a duplex oxide layer. Both the inner and outer layers were mainly composed of Cr and Fe oxide species for both samples, but the outer layer was less concentrated in Cr as compared to the inner layer. Such a distribution of the alloying elements had already been described by Wang et al. who showed that the passive film formed on 316L stainless steel was constituted of an inner Cr-enriched barrier layer [41]. A second EDS quantification was then performed without taking into account the oxygen signal: in this case, the oxygen peak was only used for the deconvolution of the energy peaks. This procedure allowed to highlight the

Table 3
XPS chemical quantification and thickness of the passive film formed in 0.5 M chloride solution under anodic potentiostatic polarisation and the underlying 17-4PH alloy for different samples. It can be noticed a high carbon concentration due to adventitious carbon. The oxide film thickness calculation is based on the ratio (I_{met}/I_{ox}) for Fe and Cr (metal and oxide) references and a Cr/Fe repartition of 20/80.

Element at%	Fe (2p)	Cr (2p)	O (1s)	Ni (2p)	Cu (2p)	Nb (3d)	Si (2p)	C (1s)	Film thickness (nm)
conventional	14.1	8.3	43.0	0.8	1.1	0.6	0.8	31.3	3.9
LBM XY	13.4	5.0	41.4	0.5	0.5	0.4	1.6	37.2	4.4
LBM XZ	15.4	5.5	42.5	0.7	0.7	0.4	1.5	33.4	4.6
LBM YZ	10.3	4.7	40.1	0.4	0.6	0.4	1.7	41.8	4.1

XPS chemical quantification and thickness of the passive film formed in 0.5M chloride solution under anodic potentiostatic polarisation and the underlying 17-4PH alloy for different samples. It can be noticed a high carbon concentration due to adventitious carbon. The oxide film thickness calculation is based on the ratio (I_{met}/I_{ox}) for Fe and Cr (metal and oxide) references and the approximate Fe/Cr ratio of 4/1.

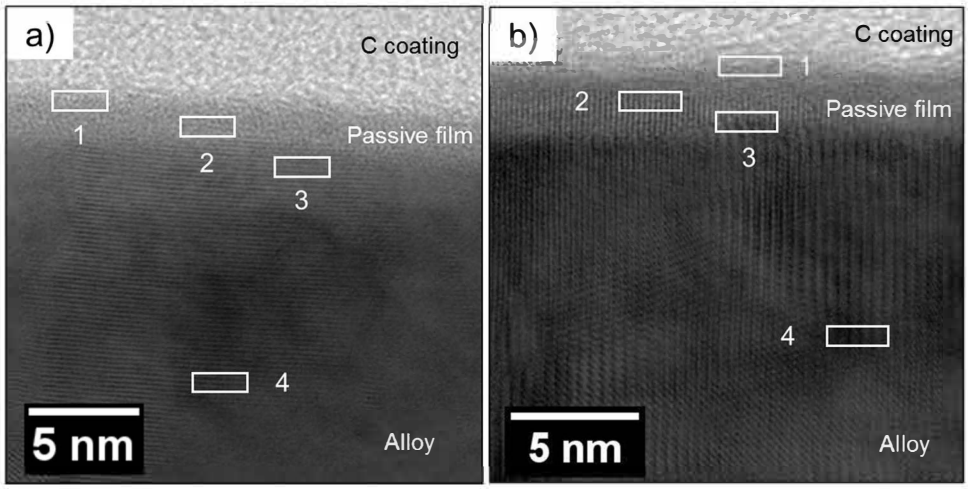

Fig. 4. STEM bright field images of the passive film formed on the conventional (a) and LBM XY (b) MSS in 0.5 M NaCl solution. White rectangles correspond to EDS analysis area (quantification are displayed in Table 4).

Table 4
EDS quantification corresponding to the EDS analysis boxes performed on conventional and LBM XY samples based on the STEM bright field imaging of Fig. 4. Quantification without taking into account the O was made in order to better follow the variation of alloying element composition between each boxes.

Composition (at. %)		Quantification with O						Quantification without O					Interpretation
	Boxes	O	Fe	Cr	Ni	Cu	Si	Fe	Cr	Ni	Cu	Si	
conventional	1	48.9	43.1	5.2	0.4	0.5	1.9	84.4	10.1	0.9	1.0	3.6	outer layer
(Fig. 4a)	2	39.6	41.0	12.1	3.2	3.0	1.1	68.0	20.0	5.4	4.9	1.8	Inner / intermediate layer
	3	7.7	69.6	15.2	4.2	2.6	0.7	75.4	16.1	4.5	2.9	0.8	alloy
	4	1.5	74.6	15.5	4.6	3.0	0.9	75.8	15.7	4.6	3.0	0.9	alloy
LBM XY	1	43.9	49.2	6.1	0.0	0.3	0.6	87.6	10.8	0.1	0.5	1.0	outer layer
(Fig. 4b)	2	42.8	43.5	9.6	1.2	1.5	1.4	76.1	16.7	2.1	2.6	2.5	inner layer
	3	18.2	56.5	14.6	4.3	4.7	1.7	69.1	17.9	5.2	5.7	2.1	interface layer
	4	0.0	75.0	16.2	4.2	3.6	1.0	75.0	16.2	4.2	3.6	1.0	alloy

EDS quantification corresponding to the EDS analysis boxes performed on conventional and LBM XY samples based on the STEM bright field imaging of Fig. 4. Quantification without taking into account the O was made in order to better follow the variation of alloying element composition between each boxes.

relative variation of the secondary alloying elements. Results thus showed that Cr, Ni and Cu atomic contents reached maximum values at the intermediate layer for the LBM XY MSS. For the conventional alloy, the Cr, Ni and Cu contents were maximum in box 2 which included both the contribution of the inner and the intermediate layers. For Cr, the global amount, i.e. including both the outer and inner layers was lower for the LBM sample, as compared to the conventional one, in agreement with previous XPS analyses. This could be linked mostly to the inner layer composition, with a significantly lower amount of Cr in the inner layer for the LBM sample as compared to the conventional one. Furthermore, Cu and Ni were detected in significantly smaller amounts in the outer layer as compared to the inner layer for the LBM XY sample and were found to segregate at the intermediate layer. For the conventional sample, it was more difficult to conclude, considering that box 2 included, as previously indicated, both the inner and the intermediate layer, even though literature data indicate that Cu and Ni should be segregated at the intermediate layer as for the LBM XY sample. Indeed, the enrichment in noble alloying elements at the interface between the passive film and the MSS could be due to the preferential dissolution of Fe species leading to a modified alloy zone at the interface [41]. Finally, Si was found in the passive film for both LBM XY and conventional samples. Results suggested that the Si amount was higher in the passive film formed on the conventional sample as compared to the LBM XY sample, even though the Si content was twice higher in the LBM matrix (Table 1). This could be explained considering that, in the LBM XY sample, a non-negligible Si content was concentrated in the Si-rich oxide inclusions generated by the manufacturing process and present in the alloy [9,44,52]. The interpretation of these results is nevertheless limited by the complexity of EDS detection of small Si amount.

To complete this analysis, elementary XPS depth profiles were performed for all the four samples. Fig. 5 shows the results for the conventional (Fig. 5a), the LBM XY (Fig. 5b) and the LBM XZ (Fig. 5c) samples; the depth profiles of LBM YZ (not plotted here) have the same evolution than those of the LBM XZ sample. The evolution of Fe, Cr, O and the Nb oxide spectra are followed from the surface (0 s etching) to the bulk alloy (> 600 s etching). Moreover, to compare the relative evolution of Cr between LBM and conventional samples, normalised ratio Cr / [O + Fe + Cr], which represents the variations of the Cr content relatively to the main elements of the passive films, was plotted versus the etching time for the four samples (Fig. 5d). This last representation was helpful to roughly identify the different layers by considering the above-mentioned EDS results relative to Cr content in both the outer and the inner layers for one part, and the Cr enrichment at the intermediate layer for the other part, in particular for the LBM XY sample. Besides, the position of the intermediate layer was also visible with the increase in Fe content in parallel with the fast drop of the O line under 10 at. % after 150 s of etching for both samples. It is of interest to mention here that the amounts of alloying elements in Fig. 5 cannot be compared easily with those given in Table 3, where the high C amount due to organic contamination disturbed the quantitative analysis. Results in Fig. 5 suggested a difference in the Cr content and distribution between the LBM XY sample on the one hand, and the conventional and LBM (X,Y)Z samples on the other hand, even though the results have to be considered carefully due to the semi quantitative characteristic of the XPS analyses, and the partial reduction of the oxides during Ar^+ etching. Hence, the Cr content for the LBM XY sample (Fig. 5b) started at 4 at.% in the outer layer, then increased through the inner layer up to the intermediate layer (maximum value of 9 at. %), confirming the Cr

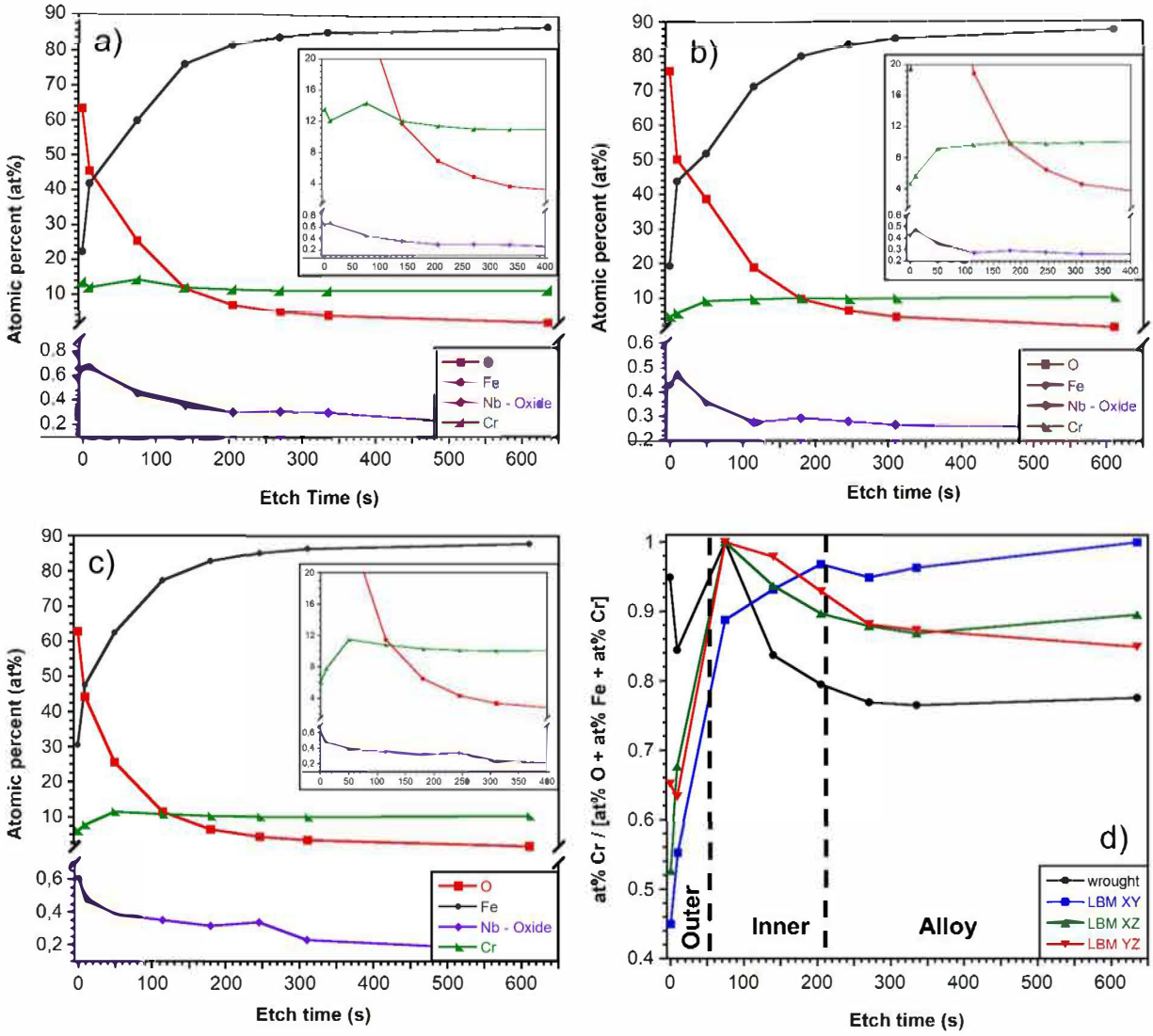

Fig. 5. XPS elementary depth profiles for conventional (a), LBM XY (b) and LBM XZ (c) samples (results for LBM YZ sample are similar to those obtained for LBM XZ sample). The variation of the elementary ratio Cr / [Cr + Fe + O] is given for the different 17-4PH MSS samples (d).

depletion in the outer layer of the passive film, in relative good agreement with STEM-EDS analyses (Fig. 4, Table 4). The Cr depletion in the outer layer was also observed for LBM XZ sample (Figs. 5c) and YZ samples (not shown here), with some slight differences in the global shape of the profiles as compared to the LBM XY sample (Fig. 5b). The Cr content increased until 12 at.% in the passive film for the LBM XZ sample (Fig. 5c). For the conventional sample, the Cr content remained at a quite constant value around 12 at.% in the passive film (Fig. 5a) with a very slight enrichment in the inner layer, which was also consistent with STEM-EDS analyses, even though a more marked Cr depletion in the outer layer had been seen with STEM-EDS analyses. Furthermore, Fig. 5d gives a relevant description of the Cr distribution in the passive films. The main result was that the maximum Cr content was observed in the inner layer for both the conventional and LBM (X,Y)Z samples, whereas it was reached in the intermediate layer for the LBM XY sample. Finally, it was of importance to note that XPS profiles showed a global Cr amount higher for the passive film formed on the conventional sample as compared to the LBM sample, in agreement with STEM-EDS results. The differences in the global Cr amount, and also in Cr distribution, through the two layers of the passive films formed on the conventional MSS for one part, and on the LBM MSS for the other part, could contribute to explain the difference in the susceptibility to stable and metastable pitting observed between the two steels. Indeed, recent work of Coelho et al. demonstrated that a higher Cr content in the passive film enhanced his stability and thus the pitting potential for the same alloy with different surface treatment [55], whereas Wang et al. showed that protective properties of the passive film was mainly attributed to its inner part [41]. On the basis of the literature, we propose that the higher susceptibility to metastable pitting observed in our previous study [44] for the LBM samples could be linked to the lower Cr amount in the passive films formed on these samples, as compared to the conventional sample. As previously indicated, this could be due to the lower martensite to austenite ratio in LBM samples as compared to the conventional sample. Furthermore, we also showed a specific behaviour of the LBM XY sample as compared to LBM (X,Y)Z samples, with some metastable pits reaching a maximal growth rate significantly higher than those formed on the conventional and LBM (X,Y)Z samples [44]. The difference should be explained by the Cr distribution inside the passive films as shown by Fig. 5d: the low Cr amount in both the outer and inner layers of the passive film formed on the LBM XY sample, as compared to both the conventional and LBM (X,Y)Z samples, should explain the result. Here also, the results could be related to the martensite to austenite ratio since we showed in previous study [44] that the amount of reversed austenite was ~8% and 12% in LBM (X,Y)Z samples and LBM XY sample, respectively. Such a difference in austenite content had been related to the anisotropic morphology of the prior

austenitic grains before the H900 heat treatment. On the contrary, the more noble pitting potentials measured for the LBM samples as compared to the conventional alloy could be due to other features of the passive film, in particular its thickness and/or defects at specific microstructural features. Indeed, as previously said, the influence of the NbC precipitates on the pitting behaviour could not be neglected. Therefore, the presence of Nb oxide in the passive film was studied, and the variation in depth of the Nb 3d spectra corresponding, as determined by XPS, to NbC_xO_y and NbO_2 was also followed. Results had to be considered carefully because of the risk of reduction during the Ar^+ sputtering and the low amount of Nb (whereas Nb has a high photo-ionisation cross section). Nevertheless, they showed a significant content of Nb oxide in the outer layer (10 s etching) followed by a slow decrease until the bulk alloy was reached for both samples. This evolution of the Nb spectrum was consistent with the presence of stable NbO_2 in the outer layer followed by a mix of NbO_x and NbC_y in the inner layer.

To summarise, the passive films formed on 17-4PH MSS under anodic polarisation in NaCl solution had a similar structure for LBM and conventional samples. They had a bilayer structure characterised by an outer layer mainly constituted of Fe oxy-hydroxide and an inner layer enriched in Cr oxide. In addition, a slight amount of Nb oxide was also detected, mainly in the outer part of the passive films. The intermediate layer between the passive film and the bulk alloy corresponded to a zone enriched in metallic alloying elements (*i.e.* Cr, Cu and Ni) which were not dissolved during the passive film growth. However, some differences could be noticed for the Cr and the Si content between conventional sample and the LBM samples. The global amount and distribution of Cr seems to be the main parameter which controls the passivity properties and so the corrosion behaviour of the different samples as previously

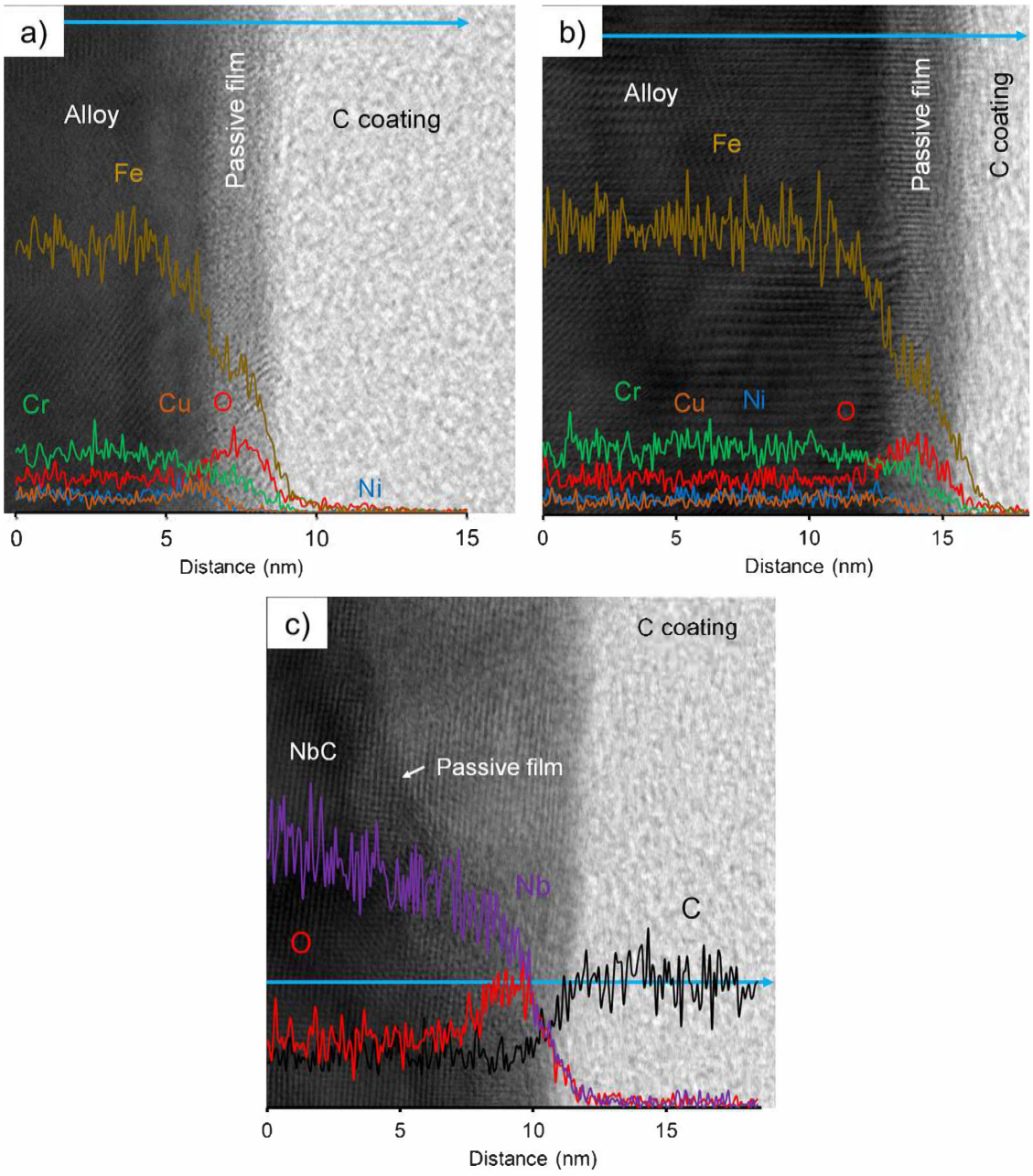

Fig. 6. STEM bright field images of the passive film formed in chloride solution a) on the conventional sample, b) on the LBM XY sample and c) on a NbC precipitate emerging at the surface on the LBM XY sample. EDS line profiles (blue arrows) are shown with the relative atomic variation of the alloying elements along the profile line. (For interpretation of the references to color in this figure legend, the reader is referred to the web version of this article.)

explained, with on the one hand differences between the conventional sample and the LBM samples, and on the other hand differences between the LBM XY and LBM (X,Y)Z samples; all the differences might be related to changes in martensite to austenite ratio. However, the slight Si enrichment in the outer layer of the passive film for the conventional sample could also contribute to explain the difference in corrosion behaviour observed in the previous work [44]. Indeed, Laurent et al. show that Si addition in 304LN SS has an indirect effect on corrosion behaviour due to Si ability to segregate at grain boundaries with other alloying species, leading to Cr-depleted area [43]. Nevertheless, the resistance to localised corrosion is also closely linked to the passive film defects. In the case of 17-4PH MSS, secondary NbC precipitates in the alloy matrix can constitute preferential pit initiation sites [44,45], likely due to differences in the passive film formed on these precipitates. Therefore the particular passive film structure at NbC precipitates had to be studied, which meant to perform local analyses.

3.3. Analysis of the passive films formed on NbC precipitates

As discussed previously, Nb 3d high-resolution XPS spectra were composed of multiple components including $Nb^{IV}O_2$ oxide and a mix of niobium-carbon-oxide NbC_xO_y (Figs. 2g and 3g). Thus, it could be suspected that NbC precipitates were oxidised and that the oxide layer formed on these specific microstructural features was different from the passive film formed on the matrix. To confirm such an hypothesis, EDS profiles were performed on STEM BF images across the passive film formed on the martensitic matrix of the conventional (Fig. 6a) and the LBM XY samples (Fig. 6b) as well as on NbC precipitates emerging at the surface of the LBM XY sample (Fig. 6c). In Fig. 6, the blue arrows indicate where the EDS profiles were performed on the images. Fig. 6a and b show that the passive film formed on the martensitic matrix is mainly composed of O, Cr and Fe for both samples. The intermediate layer can also be identified by a slight increase in the Cu and Ni signals just before reaching the passive film, especially for the conventional sample. However, Nb was not detected in the passive film formed on the martensitic matrix. On the contrary, a significant Nb signal was associated with an O peak (Fig. 6c) when the EDS profile was performed from the surface across a NbC precipitate in LBM XY sample, which showed that a specific passive film formed on NbC precipitates as suggested by XPS analysis. STEM BF (Fig. 7a and b) images of NbC precipitates

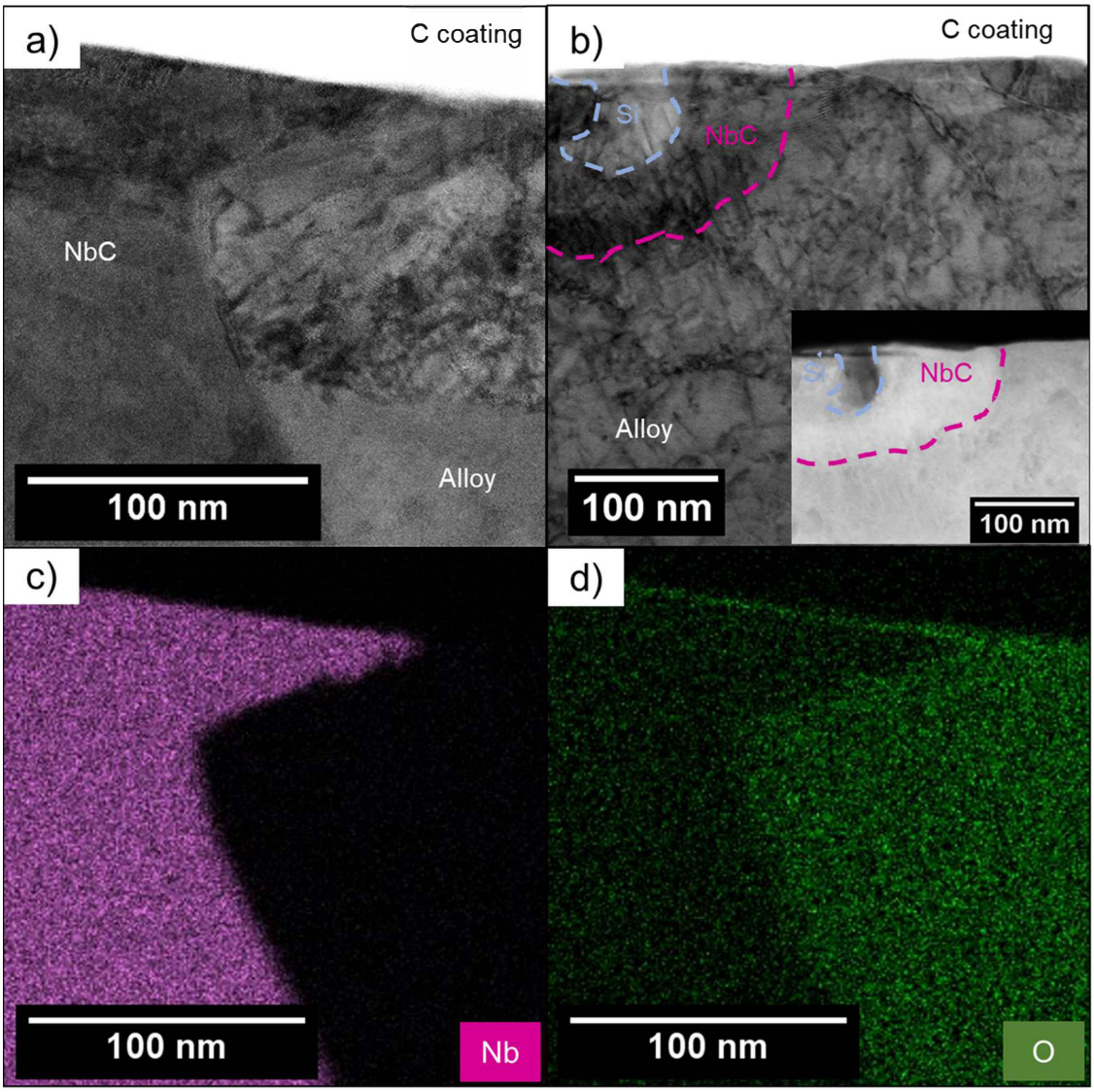

Fig. 7. a) STEM bright field image of the passive film formed on a NbC precipitate emerging at the surface on the conventional MSS sample; b) STEM bright field image on a NbC coupled with a Si-rich oxide inclusion emerging at the surface for the LBM XY MSS sample with the STEM HAADF image insert. The STEM EDS maps for c) Nb and d) O have been performed on the same area of STEM BF image a) showing a passive film formed on a NbC precipitate emerging at the surface and on the martensitic matrix.

emerging at the surface for conventional and LBM XY samples, respectively, were performed to confirm the presence of a passive film covering the NbC precipitates. It could be noticed that the NbC precipitate for LBM XY sample (Fig. 7b) was smaller than for the conventional sample and was coupled with a Si-rich oxide inclusion; this could be related to local segregation of alloying elements around the inclusions as already discussed in previous work [44]. STEM-EDS maps of Nb (Fig. 7c) and O (Fig. 7d) were performed on the STEM BF image of the conventional sample (Fig. 7a). O signal was present all along the NbC precipitate confirming that a passive film covered the whole NbC precipitate surface; furthermore, qualitative observation suggested that the passive film formed on the NbC precipitates was thinner than that formed on the martensitic matrix. Indeed, the thickness of the passive film formed on the NbC precipitates was evaluated around 1.5 nm as compared to 3 nm for the one formed on the martensitic matrix. The higher O signal measured for the martensitic matrix as compared to the NbC precipitate in the bulk alloy was certainly due to the greatest solubility of O in the interstitial site of the martensite. Similar observations were also performed for the LBM XY sample.

To summarise, the specific passive film formed on NbC precipitates emerging at the surface seems to be composed of a duplex oxide layer with a transition inner oxide NbC_xO_y and a stable $Nb^{IV}O_2$ in the outer layer. The presence of a passive film on the NbC precipitates clearly demonstrated the reactivity of those particles in NaCl solution despite their noble electrochemical behaviour [45]. As already discussed, the corrosion behaviour of the 17-4PH MSS and particularly its pitting corrosion susceptibility could be, at least partially, explained by considering the NbC precipitates which could act as preferential pit initiation and propagation sites [44]. The results obtained in the present study, with different chemical composition and thickness of the passive film formed on the NbC precipitates as compared to the matrix, were relevant with such a hypothesis. As known, the pitting corrosion behaviour is controlled by the defects in the passive film, i.e. at grain boundaries or precipitates, which can act as preferential sites for passive film breakdown assisted by Cl^- species. Results obtained in the present study are in agreement with those literature data. Then, we attribute the difference in stable pitting corrosion behaviour between LBM and conventional samples to the difference in proportion and size of the NbC precipitates, despite the passive film formed on the NbC precipitates for the two MSSs are similar. However, even though our previous TEM observations qualitatively showed similar thickness for the passive films formed on the martensitic matrix for both MSSs, slight differences in this parameter can also contribute to the difference in corrosion behaviour between the LBM and the conventional samples. Therefore, more detailed attention was paid to this specific parameter.

3.4. Thickness of the passive film

To obtain reliable thickness values of the passive film formed on the conventional and the LBM samples, calculations based on XPS spectral intensities were compared to the thickness measured on TEM images. The thickness estimation with XPS (Table 3) was based on a formula using reference samples for Cr and Fe metals and oxides [56,57]:

$$d_x = \lambda_x^{oxide} \sin\theta \ln\left[\left(\frac{D^{alloy}}{D^{oxide}}\frac{\lambda_x^{alloy}}{\lambda_x^{oxide}}\frac{I_x^{oxide}}{I_x^{alloy}}\frac{I_{ref}^{alloy}}{I_{ref}^{oxide}}\right)+1\right] \quad (2)$$

with d_x the thickness of the oxide layer for the element x in nm, λ_x^y the inelastic mean free path of photoelectrons emitted by the core level of the element x in the environment y in nm, θ the take-off angle of the apparatus (90°) in degree, D^{alloy} the density of the 17-4PH measured by hydrostatic weighing (7.7 g cm^{-3} for the LBM sample and 7.8 g cm^{-3} for the conventional sample), D^{oxide} the density of the Cr_2O_3 and Fe_2O_3 taken at 5.2 g cm^{-3}, I_x^y the intensity of the photoelectrons emitted from the element x at the chemical state y, and I_{ref}^y the intensity of the photoelectrons emitted from the reference of Cr or Fe at the chemical state y. The oxide state coming from the XPS high-resolution spectra includes oxide and hydroxide of an element. Finally, the thickness of the passive film was calculated using the approximate Fe/Cr ratio of 4/1 (Table 4, quantification without O) deduced from the STEM-EDS results:

$$d_{passive\ film} = 0.2d_{Cr} + 0.8d_{Fe} \quad (3)$$

where d_{Cr} and d_{Fe} were the oxide thicknesses in nm calculated for Cr and Fe oxides, respectively. The results are displayed in Table 3 and show similar thickness values for all the samples around 4 nm, which is in the expected order of magnitude for a passive film formed on stainless steel [40–42]. Nevertheless, it appeared that the passive film formed on the conventional sample was slightly thinner than that formed on all the LBM samples. A slight difference was also observed between the different LBM samples. To confirm the result, additional measurements were performed using TEM, and the thickness of the passive films formed at different zones (at least 10 measurements) was measured by TEM observations. Results showed that the thickness of the passive film formed on the martensitic matrix was 2.4 ± 0.1 nm and 3.0 ± 0.1 nm for the conventional sample and the LBM XY sample, respectively. The values were slightly lower than those estimated by XPS; the differences can be explained by the different surface regions probed by the two techniques (50 nm^2 in TEM vs. 4000 nm^2 in XPS), and/or limitations of the use of Eq. (2). Overall, both technique are in the same order of magnitude. Moreover, the thickness of the passive film evaluated from TEM observations was weaker for the conventional sample than for the LBM XY sample, which is in agreement with the values derived from XPS. Finally, additional measurements using TEM observations were also performed to evaluate the thickness of the passive film formed on the NbC precipitates; results showed that the passive film formed on NbC precipitates was thinner, with thickness values twice smaller (between 1.1 and 1.6 nm) than those measured on the martensitic matrix. The thinner passive film upon the NbC precipitates, combined with a possible galvanic couple between those precipitates and the martensitic matrix [45], confirmed the deleterious effect of NbC precipitates on the stable pitting corrosion behaviour. As previously shown, the pitting potential of the LBM samples was nobler than that of the conventional sample; this was related to smaller and less numerous NbC precipitates in the LBM samples as compared to the conventional MSS [44]. The better resistance to stable pitting of the LBM sample was therefore assumed to originate from a decrease in the amount of possible initiation sites for pitting corrosion as compared to the conventional sample. However, the greater intensity of the current transients generated on the LBM samples, i.e. the higher susceptibility to metastable pitting of LBM MSS, could be linked to the lower Cr content of the passive films formed on LBM samples as compared to the conventional MSS, which decreased capability to repassivation of LBM passive films.

Thereby, a schematic view of the passive film formed on 17-4PH MSS in NaCl solution could be drawn based on the results obtained from TEM and XPS analyses (Fig. 8). The homogenous passive film covering the whole surface, i.e. the martensitic matrix, was disrupted by the presence of NbC precipitates, which were covered by a thinner oxide film with a significantly different chemical composition. In that sense, those results represent consolidated proof of the deleterious role of NbC precipitates towards stable pitting corrosion behaviour in 17-4 PH MSS. However, the role of the manufacturing defects (e.g. gas pores, lack-of-fusion pores, Si-rich inclusions…) on the pitting corrosion behaviour and so on the passive structure, cannot be neglected, but it was not the focus of the present study.

4. Conclusions

The passive films formed in NaCl solution on a LBM and a conventional 17-4PH MSS, treated with the same annealing heat treatment followed by H900 ageing, were characterised using combined STEM-

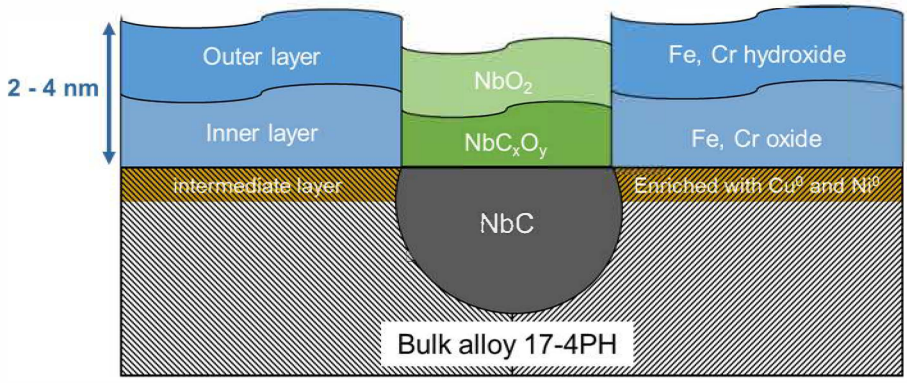

Fig. 8. Diagram representative of the passive film formed on 17-4PH MSS in chloride solution.

EDS and XPS analyses. Their thickness, chemical composition and structure were thoroughly described and main outputs can be drawn:

- The passive films formed on the martensitic matrix for LBM and conventional MSS have a similar structure, i.e. a duplex oxy-hydroxide layer followed by an intermediate layer enriched in alloying elements before reaching the alloy. The outer oxide layer is mainly composed of Fe oxide and hydroxide, whereas the inner layer is enriched in CrIII species in addition to the Fe oxide; finally, the intermediate layer has the composition of the alloy with an enrichment in metallic Ni and Cu mainly, but also in Cr species. The global Cr content is higher in the passive film formed on the conventional MSS as compared to the passive film formed on LBM MSSs; this should be explained by the lower martensite to reversed austenite ratio for LBM MSSs.
- At the NbC precipitates, the passive film is composed of an oxide bilayer with an inner two-phase layer of NbC and Nb oxi-carbide and an outer stable single-phase NbO2 oxide. The passive film formed on the NbC precipitates is found to be thinner than the passive film formed on the martensitic matrix.
- The differences in pitting corrosion resistance between LBM and conventional 17-4PH MSSs are attributed to differences in the chemical composition and structure (i.e. influence of defects) of the passive films formed on the two MSSs. The less defective structure of the passive films formed on LBM samples, due to smaller and less numerous NbC precipitates, contributes to an increase of the resistance to stable pitting corrosion of these samples, with more positive pitting potentials as compared to conventional MSS. However, the lower amount of Cr in the passive films formed on the LBM samples, as compared to the conventional sample, could contribute to explain their lower repassivation capability, leading to a stronger susceptibility to metastable pitting. Finally, the differences in thickness observed between the passive films formed on the martensitic matrix for the both MSSs could not be neglected.

Data availability

The raw/processed data required to reproduce these findings cannot be shared at this time as the data also forms part of an ongoing study.

Author statement

I certify that the work described in the manuscript has not been published previously, that it is not under consideration for publication elsewhere, that its publication is approved by all authors and tacitly or explicitly by the responsible authorities where the work was carried out, and that, if accepted, it will not be published elsewhere in the same form, in English or in any other language, including electronically without the written consent of the copyright-holder.

A. Barroux: Investigations. Formal analysis. Validation. Visualization. Methodology. Data curation. Writing-original draft. Writing-Review & Editing. T. Duguet: Investigations (for XPS analyses). Formal analysis (for XPS results). Validation (for XPS results). Methodology (for XPS analyses). Writing-Review & Editing. N. Ducommun: Funding acquisition (financial support). Resources (Materials). Project administration. Supervision. Writing-Review & Editing. E. Nivet: Funding acquisition (financial support). Resources (Materials). Project administration. Supervision. Writing-Review & Editing. J. Delgado: Funding acquisition (financial support). Resources (Materials). Project administration. Supervision. Writing-Review & Editing. L. Laffont: Investigations (for TEM analyses). Formal analyses (for TEM). Methodology. Supervision. Validation. Conceptualization. Data curation. Writing-original draft. Writing-Review & Editing. C. Blanc: Funding acquisition. Methodology. Project administration. Supervision. Validation. Conceptualization. Data curation. Writing-original draft. Writing-Review & Editing.

Declaration of Competing Interest

The authors declare that they have no known competing financial interests or personal relationships that could have appeared to influence the work reported in this paper.

Acknowledgements

The authors thank the ANRT for their financial support (Adrien Barroux's PhD thesis). We are thankful to Jérôme Esvan (CIRIMAT, Toulouse, FR) for his occasional help and sharing of expertise in XPS.

References

[1] G. Yeli, M.A. Auger, K. Wilford, G.D.W. Smith, P.A.J. Bagot, M.P. Moody, Sequential nucleation of phases in a 17-4PH steel: Microstructural characterisation and mechanical properties, Acta Mater. 125 (2017) 38–49, https://doi.org/10.1016/j.actamat.2016.11.052.
[2] U.K. Viswanathan, S. Banerjee, R. Krishnan, Effects of aging on the microstructure of 17-4 PH stainless steel, Mater. Sci. Eng. A 104 (1988) 181–189, https://doi.org/10.1016/0025-5416(88)90420-X.
[3] C.N. Hsiao, C.S. Chiou, J.R. Yang, Aging reactions in a 17-4 PH stainless steel, Mater. Chem. Phys. 74 (2002) 134–142, https://doi.org/10.1016/S0254-0584(01)00460-6.
[4] H.R. Habibi Bajguirani, The effect of ageing upon the microstructure and mechanical properties of type 15-5 PH stainless steel, Mater. Sci. Eng. A 338 (2002) 142–159, https://doi.org/10.1016/S0921-5093(02)00062-X.
[5] L. Couturier, F. De Geuser, M. Descoins, A. Deschamps, Evolution of the microstructure of a 15-5PH martensitic stainless steel during precipitation hardening heat treatment, Mater. Des. 107 (2016) 416–425, https://doi.org/10.1016/j.matdes.2016.06.068.
[6] T. Lebrun, K. Tanigaki, K. Horikawa, H. Kobayashi, Strain rate sensitivity and mechanical anisotropy of selective laser melted 17-4 PH stainless steel, Mech. Eng. J. 1 (2014), https://doi.org/10.1299/mej.2014smm0049. SMM0049–SMM0049.
[7] A. Yadollahi, N. Shamsaei, S.M. Thompson, A. Elwany, L. Bian, Effects of building orientation and heat treatment on fatigue behavior of selective laser melted 17-4

PH stainless steel, Int. J. Fatigue. 94 (2017) 218–235, https://doi.org/10.1016/j.ijfatigue.2016.03.014. Part 2.
[8] S. Cheruvathur, E.A. Lass, C.E. Campbell, Additive manufacturing of 17-4 PH stainless steel: post-processing heat treatment to achieve uniform reproducible microstructure, JOM 68 (2016) 930–942, https://doi.org/10.1007/s11837-015-1754-4.
[9] X. Lou, P.L. Andresen, R.B. Rebak, Oxide inclusions in laser additive manufactured stainless steel and their effects on impact toughness and stress corrosion cracking behavior, J. Nucl. Mater. 499 (2018) 182–190, https://doi.org/10.1016/j.jnucmat.2017.11.036.
[10] L. Carneiro, B. Jalalahmadi, A. Ashtekar, Y. Jiang, Cyclic deformation and fatigue behavior of additively manufactured 17–4 PH stainless steel, Int. J. Fatigue. 123 (2019) 22–30, https://doi.org/10.1016/j.ijfatigue.2019.02.006.
[11] B. AlMangour, J.-M. Yang, Improving the surface quality and mechanical properties by shot-peening of 17-4 stainless steel fabricated by additive manufacturing, Mater. Des. 110 (2016) 914–924, https://doi.org/10.1016/j.matdes.2016.08.037.
[12] H. Gu, H. Gong, D. Pal, K. Rafi, T. Starr, B. Stucker, Influences of energy density on porosity and microstructure of selective laser melted 17-4PH stainless steel, in: 2013 Solid Free. Fabr. Symp., 2013: p. 474. http://sffsymposium.engr.utexas.edu/Manuscripts/2013/2013-37-Gu.pdf.
[13] A. Kudzal, B. McWilliams, C. Hofmeister, F. Kellogg, J. Yu, J. Taggart-Scarff, J. Liang, Effect of scan pattern on the microstructure and mechanical properties of Powder Bed Fusion additive manufactured 17-4 stainless steel, Mater. Des. 133 (2017) 205–215, https://doi.org/10.1016/j.matdes.2017.07.047.
[14] R. Rashid, S.H. Masood, D. Ruan, S. Palanisamy, R.A. Rahman Rashid, M. Brandt, Effect of scan strategy on density and metallurgical properties of 17-4PH parts printed by selective laser melting (SLM), J. Mater. Process. Technol. 249 (2017) 502–511, https://doi.org/10.1016/j.jmatprotec.2017.06.023.
[15] Y. Sun, R.J. Hebert, M. Aindow, Non-metallic inclusions in 17-4PH stainless steel parts produced by selective laser melting, Mater. Des. 140 (2018) 153–162, https://doi.org/10.1016/j.matdes.2017.11.063.
[16] H. Irrinki, M. Dexter, B. Barmore, R. Enneti, S. Pasebani, S. Badwe, J. Stitzel, R. Malhotra, S.V. Atre, Effects of powder attributes and laser powder bed fusion (L-PBF) process conditions on the densification and mechanical properties of 17-4 PH stainless steel, JOM 68 (2016) 860–868, https://doi.org/10.1007/s11837-015-1770-4.
[17] L.E. Murr, E. Martinez, J. Hernandez, S. Collins, K.N. Amato, S.M. Gaytan, P. W. Shindo, Microstructures and properties of 17-4 PH stainless steel fabricated by selective laser melting, J. Mater. Res. Technol. 1 (2012) 167–177, https://doi.org/10.1016/S2238-7854(12)70029-7.
[18] S.D. Meredith, J.S. Zuback, J.S. Keist, T.A. Palmer, Impact of composition on the heat treatment response of additively manufactured 17–4 PH grade stainless steel, Mater. Sci. Eng. A 738 (2018) 44–56, https://doi.org/10.1016/j.msea.2018.09.066.
[19] M. Alnajjar, F. Christien, V. Barnier, C. Bosch, K. Wolski, M A.D. Fortes, Telling, Influence of microstructure and manganese sulfides on corrosion resistance of selective laser melted 17-4 PH stainless steel in acidic chloride medium, Corros. Sci. 168 (2020), 108585, https://doi.org/10.1016/j.corsci.2020.108585.
[20] L. Wang, C. Dong, C. Man, D. Kong, K. Xiao, X. Li, Enhancing the corrosion resistance of selective laser melted 15-5PH martensite stainless steel via heat treatment, Corros. Sci. 166 (2020), 108427, https://doi.org/10.1016/j.corsci.2019.108427.
[21] M.J. Tobar, J.M. Amado, J. Montero, A. Yáñez, A study on the effects of the use of gas or water atomized AISI 316L steel powder on the corrosion resistance of laser deposited material, Phys. Procedia 83 (2016) 606–612, https://doi.org/10.1016/j.phpro.2016.08.063.
[22] Q. Chao, V. Cruz, S. Thomas, N. Birbilis, P. Collins, A. Taylor, P.D. Hodgson, D. Fabijanic, On the enhanced corrosion resistance of a selective laser melted austenitic stainless steel, Scr. Mater. 141 (2017) 94–98., https://doi.org/10.1016/j.scriptamat.2017.07.037.
[23] M. Laleh, A.E. Hughes, S. Yang, J. Li, W. Xu, I. Gibson, M.Y. Tan, Two and three-dimensional characterisation of localised corrosion affected by lack-of-fusion pores in 316L stainless steel produced by selective laser melting, Corros. Sci. 165 (2020), 108394, https://doi.org/10.1016/j.corsci.2019.108394.
[24] M. Laleh, A.E. Hughes, W. Xu, P. Cizek, M.Y. Tan, Unanticipated drastic decline in pitting corrosion resistance of additively manufactured 316L stainless steel after high-temperature post-processing, Corros. Sci. 165 (2020), 108412, https://doi.org/10.1016/j.corsci.2019.108412.
[25] D. Nakhaie, M.H. Moayed, Pitting corrosion of cold rolled solution treated 17-4 PH stainless steel, Corros. Sci. 80 (2014) 290–298, https://doi.org/10.1016/j.corsci.2013.11.039.
[26] S.-Y. Lu, K.-F. Yao, Y.-B. Chen, M.-H. Wang, N. Chen, X.-Y. Ge, Effect of quenching and partitioning on the microstructure evolution and electrochemical properties of a martensitic stainless steel, Corros. Sci. 103 (2016) 95–104, https://doi.org/10.1016/j.corsci.2015.11.010.
[27] H. Luo, Q. Yu, C. Dong, G. Sha, Z. Liu, J. Liang, L. Wang, G. Han, X. Li, Influence of the aging time on the microstructure and electrochemical behaviour of a 15-5PH ultra-high strength stainless steel, Corros. Sci. 139 (2018) 185–196, https://doi.org/10.1016/j.corsci.2018.04.032.
[28] V. Vignal, S. Ringeval, S. Thiébaut, K. Tabalaiev, C. Dessolin, O. Heintz, F. Herbst, R. Chassagnon, Influence of the microstructure on the corrosion behaviour of low-carbon martensitic stainless steel after tempering treatment, Corros. Sci. 85 (2014) 42–51, https://doi.org/10.1016/j.corsci.2014.03.036.
[29] S.S.M. Tavares, F.J. da Silva, C. Scandian, G.F. da Silva, H.F.G. de Abreu, Microstructure and intergranular corrosion resistance of UNS S17400 (17-4PH) stainless steel, Corros. Sci. 52 (2010) 3835–3839, https://doi.org/10.1016/j.corsci.2010.07.016.
[30] J. Soltis, Passivity breakdown, pit initiation and propagation of pits in metallic materials – review, Corros. Sci. 90 (2015) 5–22, https://doi.org/10.1016/j.corsci.2014.10.006.
[31] M. Urquidi, D.D. Macdonald, Solute-vacancy interaction model and the effect of minor alloying elements on the initiation of pitting corrosion, J. Electrochem. Soc. 132 (1985) 555, https://doi.org/10.1149/1.2113886.
[32] C.Y. Chao, L.F. Lin, D.D. Macdonald, A point defect model for anodic passive films: I. Film growth kinetics, J. Electrochem. Soc. 128 (1981) 1187, https://doi.org/10.1149/1.2127591.
[33] D.D. Macdonald, On the tenuous nature of passivity and its role in the isolation of HLNW, J. Nucl. Mater. 379 (2008) 24–32, https://doi.org/10.1016/j.jnucmat.2008.06.004.
[34] D.D. Macdonald, The history of the point defect model for the passive state: a brief review of film growth aspects, Electrochimica Acta 56 (2011) 1761–1772, https://doi.org/10.1016/j.electacta.2010.11.005.
[35] P. Marcus, V. Maurice, H.-H. Strehblow, Localized corrosion (pitting): a model of passivity breakdown including the role of the oxide layer nanostructure, Corros. Sci. 50 (2008) 2698–2704, https://doi.org/10.1016/j.corsci.2008.06.047.
[36] H.-H. Strehblow, Passivity of metals studied by surface analytical methods, a review, Electrochimica Acta 212 (2016) 630–648, https://doi.org/10.1016/j.electacta.2016.06.170.
[37] O. Lavigne, C. Alemany-Dumont, B. Normand, P. Delichère, A. Descamps, Cerium insertion in 316L passive film: effect on conductivity and corrosion resistance performances of metallic bipolar plates for PEM fuel cell application, Surf. Coat. Technol. 205 (2010) 1870–1877, https://doi.org/10.1016/j.surfcoat.2010.08.051.
[38] H. Ogawa, H. Omata, I. Itoh, H. Okada, Auger electron spectroscopic and electrochemical analysis of the effect of alloying elements on the passivation behavior of stainless steels, Corrosion 34 (1978) 52–60, https://doi.org/10.5006/0010-9312-34.2.52.
[39] E. Gardin, S. Zanna, A. Seyeux, A. Allion-Maurer, P. Marcus, Comparative study of the surface oxide films on lean duplex and corresponding single phase stainless steels by XPS and ToF-SIMS, Corros. Sci. 143 (2018) 403–413, https://doi.org/10.1016/j.corsci.2018.08.009.
[40] E. Gardin, S. Zanna, A. Seyeux, A. Allion-Maurer, P. Marcus, XPS and ToF-SIMS characterization of the surface oxides on lean duplex stainless steel – global and local approaches, Corros. Sci. 155 (2019) 121–133, https://doi.org/10.1016/j.corsci.2019.04.039.
[41] Z. Wang, F. Di Franco, A. Seyeux, S. Zanna, V. Maurice, P. Marcus, Passivation-induced physicochemical alterations of the native surface oxide film on 316L austenitic stainless steel, J. Electrochem. Soc. 166 (2019) C3376–C3388, https://doi.org/10.1149/2.0321911jes.
[42] K. Oh, S. Ahn, K. Eom, K. Jung, H. Kwon, Observation of passive films on Fe–20Cr–xNi (x=0, 10, 20wt.%) alloys using TEM and Cs-corrected STEM–EELS, Corros. Sci 79 (2014) 34–40, https://doi.org/10.1016/j.corsci.2013.10.023.
[43] B. Laurent, N. Gruet, B. Gwinner, F. Miserque, K. Rousseau, K. Ogle, The kinetics of transpassive dissolution chemistry of stainless steels in nitric acid: the impact of Si, Electrochimica Acta 258 (2017) 653–661, https://doi.org/10.1016/j.electacta.2017.11.110.
[44] A. Barroux, N. Ducommun, E. Nivet, L. Laffont, C. Blanc, Pitting corrosion of 17-4PH stainless steel manufactured by laser beam melting, Corros. Sci. 169 (2020), 108594, https://doi.org/10.1016/j.corsci.2020.108594.
[45] R.N. Clark, J. Searle, T.L. Martin, W.S. Walters, G. Williams, The role of niobium carbides in the localised corrosion initiation of 20Cr-25Ni-Nb advanced gas-cooled reactor fuel cladding, Corros. Sci. 165 (2020), 108365, https://doi.org/10.1016/j.corsci.2019.108365.
[46] X. Yue, L. Zhang, Y. Hua, J. Wang, N. Dong, X. Li, S. Xu, A. Neville, Revealing the superior corrosion protection of the passive film on selective laser melted 316L SS in a phosphate-buffered saline solution, Appl. Surf. Sci. 529 (2020), 147170.
[47] M.C. Biesinger, L.W.M. Lau, A.R. Gerson, R.St.C. Smart, Resolving surface chemical states in XPS analysis of first row transition metals, oxides and hydroxides: Sc, Ti, V, Cu and Zn, Appl. Surf. Sci. 257 (2010) 887–898, https://doi.org/10.1016/j.apsusc.2010.07.086.
[48] M.C. Biesinger, B.P. Payne, A.P. Grosvenor, L.W.M. Lau, A.R. Gerson, R.St. C. Smart, Resolving surface chemical states in XPS analysis of first row transition metals, oxides and hydroxides: Cr, Mn, Fe, Co and Ni, Appl. Surf. Sci. 257 (2011) 2717–2730, https://doi.org/10.1016/j.apsusc.2010.10.051.
[49] G. Deroubaix, P. Marcus, X-ray photoelectron spectroscopy analysis of copper and zinc oxides and sulphides, Surf. Interface Anal. 18 (1992) 39–46, https://doi.org/10.1002/sia.740180107.
[50] A. OrjuelaG, R. Rincón, J.J. Olaya, Corrosion resistance of niobium carbide coatings produced on AISI 1045 steel via thermo-reactive diffusion deposition, Surf. Coat. Technol. 259 (2014) 667–675, https://doi.org/10.1016/j.surfcoat.2014.10.012.
[51] A. Gupta, M. Mittal, M.K. Singh, S.L. Suib, O.P. Pandey, Low temperature synthesis of NbC/C nano-composites as visible light photoactive catalyst, Sci. Rep. 8 (2018) 13597, https://doi.org/10.1038/s41598-018-31989-z.
[52] D. Kong, X. Ni, C. Dong, L. Zhang, C. Man, J. Yao, K. Xiao, X. Li, Heat treatment effect on the microstructure and corrosion behavior of 316L stainless steel fabricated by selective laser melting for proton exchange membrane fuel cells, Electrochimica Acta 276 (2018) 293–303, https://doi.org/10.1016/j.electacta.2018.04.188.
[53] M. Långberg, F. Zhang, E. Grånäs, C. Örnek, J. Cheng, M. Liu, C. Wiemann, A. Gloskovskii, T.F. Keller, C. Schlueter, S. Kulkarni, H. Noei, D. Lindell, U. Kivisäkk, E. Lundgren, A. Stierlec, J. Pan, Lateral variation of the native passive

film on super duplex stainless steel resolved by synchrotron hard X-ray photoelectron emission microscopy, Corros. Sci. 174 (2020), 108841, https://doi.org/10.1016/j.corsci.2020.108841.
[54] J. Yao, D.D. Macdonald, C. Dong, Passive film on 2205 duplex stainless steel studied by photo-electrochemistry and ARXPS methods, Corros. Sci. 146 (2019) 221–232, https://doi.org/10.1016/j.corsci.2018.10.020.
[55] L.B. Coelho, S. Kossman, A. Mejias, X. Noirfalise, A. Montagne, A. Van Gorp, M. Poorteman, M.-G. Olivier, Mechanical and corrosion characterization of industrially treated 316L stainless steel surfaces, Surf. Coat. Technol. 382 (2020), 125175, https://doi.org/10.1016/j.surfcoat.2019.125175.
[56] D.A. Cole, J.R. Shallenberger, S.W. Novak, R.L. Moore, M.J. Edgell, S.P. Smith, C. J. Hitzman, J.F. Kirchhoff, E. Principe, W. Nieveen, F.K. Huang, S. Biswas, R. J. Bleiler, K. Jones, SiO2 thickness determination by x-ray photoelectron spectroscopy, Auger electron spectroscopy, secondary ion mass spectrometry, Rutherford backscattering, transmission electron microscopy, and ellipsometry, J. Vac. Sci. Technol. B 18 (2000) 5, https://doi.org/10.1116/1.591208.
[57] B.R. Strohmeier, An ESCA method for determining the oxide thickness on aluminum alloys, Surf. Interface Anal. 15 (1990) 51–56, https://doi.org/10.1002/sia.740150109.